Optimization of a direct detection UV wind lidar architecture for 3D wind reconstruction at high altitude

Thibault Boulant[1], Tomline Michel[1], and Matthieu Valla[1]

[1]DOTA, ONERA, Université Paris Saclay, F-91123 Palaiseau - France

Correspondence: Boulant (thibault.boulant@onera.fr)

Abstract.

An architecture for a UV wind lidar dedicated to measuring vertical and lateral wind in front of an aircraft for gust load alleviation is presented. To optimize performance and robustness, it includes a fiber laser architecture and a Quadri Mach-Zehnder (QMZ) interferometer with a robust design to spectrally analyze the backscattered light. Different lidar param-
5 eters have been selected to minimize the standard deviation of wind speed measurement projected onto the laser axis, calculated through end-to-end simulations of the instrument. The optimization involves selecting an emission/reception telescope to maximize the amount of collected photons backscattered between 100 m and 300 m, a background filter to reduce noise from the scene, and photo-multiplier tubes (PMT) to minimize detection noise. Simulations were performed to evaluate lidar performance as a function of laser parameters. This study led to the selection of three laser architectures:
10 a commercial solid-state laser, a design of a fiber laser, and a hybrid fiber laser resulting in standard deviations of 0.18 m/s, 0.17 m/s, and 0.09 m/s, respectively, at 10 km of altitude. To reconstruct the vertical and lateral wind on the flight path, the lidar is addressed to four different directions to measure four different projections of the wind. We calculate analytically (and validate through simulations) the addressing angle with respect to the flight direction that minimizes the root mean squared error (RMSE) between the reconstructed vertical and lateral wind components and the actual ones, assuming tur-
15 bulence that follows the Von Karman turbulence model. We found that the optimum angle for an estimation at 100 m is about 50°, resulting in an improvement of about 50% compared to an angle of 15°-20° typically used in current studies.

1 Introduction

Altitude air flow velocity measurements with atmospheric lidar have various applications, including weather forecasting (Baker et al., 1995, 2014; Bruneau and Pelon, 2021; Witschas et al., 2022), determining true air speed from aircraft (Augere
20 et al., 2016), analyzing wind fields around High Altitude Platforms (Karabulut Kurt et al., 2021), and turbulence detection for Gust Load Alleviation (GLA) (Regan and Jutte, 2012; Fournier et al., 2022). GLA involves actively reducing the loads caused by air flow velocity on wings using actuators that modify the aerodynamic profile of the aircraft based on the direction and strength of the encountered wind. While this method is not novel and has been employed previously with detectors measuring turbulence near the aircraft structure, the use of lidar allows for measuring the wind structure in advance (referred
25 to as feed-forward GLA), providing time for actuators to respond to the turbulence encountered. This approach has the

potential to significantly enhance the performance of such a system. Implementing this method requires measuring the variation of vertical and lateral wind velocity typically 100 m - 200 m ahead of the aircraft. Feed-forward GLA helps reduce constraints on wing resistance during the aircraft design phase, enabling the use of longer wings or reducing wing weight to decrease aircraft fuel consumption. In addition, it will limit aircraft vibrations, particularly the effects of air pockets that

30   can hurt passengers. For this measurement, a direct-detection UV lidar optimized for molecular scattering is the optimal choice, as the presence of molecules is guaranteed at all altitudes, and the Gust Load Alleviation (GLA) system is intended to operate throughout the entire flight. In such lidar systems, a laser beam is directed into the atmosphere, and the wind velocity projected onto the laser propagation axis is determined by analyzing the frequency shift of the backscattered light induced by molecule velocity (Doppler effect). This shift is measured using a spectral analyzer. The use of UV wavelengths

35   maximizes the molecular signal, as Rayleigh scattering is proportional to $1/\lambda^4$, where λ is the laser wavelength. To spatially resolve the measurement, laser pulses are employed, so that the signal at time t (with pulse emission at t = 0 s) corresponds to a signal reflected at range r = ct/2, where c is the speed of light. To determine the 3D wind, the laser must be directed along multiple angles relative to the flight path to reconstruct the vertical and lateral wind components.

The spectral analyzer is a critical component for lidar performance. A first method involves measuring two signals corre-

40   sponding to the backscattered light passing through two narrow bandwidth filters positioned on each side of the measured Rayleigh spectrum. Changes in the spectrum position due to molecule velocities alter the intensity ratio of the two signals (approximately linearly), allowing for the retrieval of the projected velocity (Garnier and Chanin, 1992). The primary limitation of this analyzer is that atmospheric temperature, pressure, and the presence of particles can alter the spectrum's shape, introducing biases during wind speed reconstruction. A second method involves interfering the backscat-

45   tered light with itself by introducing a delay (induced by an optical path difference - OPD) between the two paths of the interferometer. In this case, the interference intensity is used to determine the phase difference between the two beams, which depends linearly on the frequency of the backscattered light. However, this intensity depends on several parameters: $I_{OPD} = A(1 + M\cos\Delta\varphi_{OPD})$ where $A = TI_0$, T is the global transmission of the interferometer (i.e., the multiplication and addition of transmissions and reflections of the optics), I_0 is the intensity of the input light, M is the contrast of the

50   interference when varying OPD, $\Delta\varphi_{OPD} = \Delta\varphi_{0,OPD} + \delta\varphi_{OPD}$ is the phase difference between the two beams, $\Delta\varphi_{0,OPD}$ is the phase difference for the laser frequency, and $\delta\varphi_{OPD}$ is the phase difference induced by the molecule velocity. The phase $\Delta\varphi_{0,OPD}$ is determined by sending a sample of the laser pulse into the interferometer. To deduce the three other parameters (A, M, and $\delta\varphi_{OPD}$), measurements are performed for several OPDs separated by less than a wavelength to determine the interference oscillation pattern [i.e., $\cos(\Delta\varphi_{OPD})$]. For this method, different instruments have been developed, including a

55   Mach-Zehnder (MZ), a QMZ (Bruneau, 2001), a fringe imaging Michelson (FIM) (Cézard et al., 2009; Herbst and Vrancken, 2016), and a fringe imaging Mach-Zehnder interferometer (FIMZ) (Bruneau, 2002). The MZ provides the lower error on the wind speed but only gives 2 measurements for three parameters (A, M, and $\delta\varphi$), so one parameter (typically M) needs to be determined independently, and the error made on this parameter introduces biases in the wind speed measurement. Additionally, to minimize errors with the MZ, the wavelength of the laser and the OPD of the interferometer need to fulfill

60   OPD = $m\lambda_0$ (with m an integer) (Bruneau and Pelon, 2021), requiring additional systems to lock the laser wavelength at the
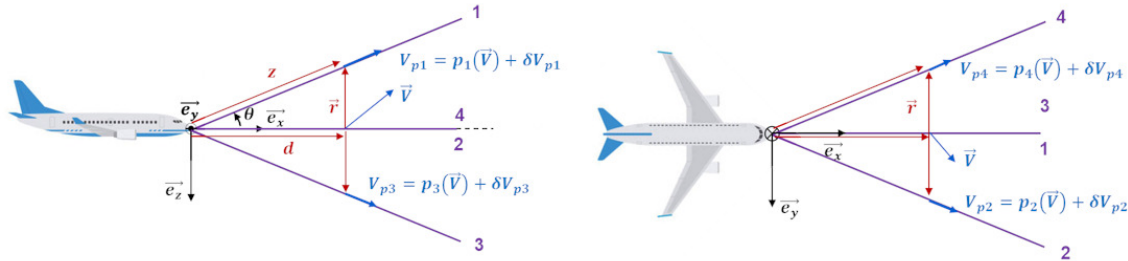
Figure 1. Measurement geometry of the reconstruction with the linear least square method with four axis. The lidar is located in the nose of the plane. d is the range between the lidar and the estimation point on the flight path, z the range of the point of the projections from the lidar, *r* the displacement vector between the projections point and the estimation point.

intersection of the two transmission curves. The QMZ, the FIM, and the FIMZ interferometers measure more than three values of OPD, allowing the retrieval of the three parameters without any assumptions (at the cost of a factor $\sqrt{2}$ increase in statistical error and do not require laser stabilization). Moreover, atmospheric parameters such as temperature, pressure, and the backscatter ratio do not produce bias. In the case of the FIM and FIMZ, the fringes need to be imaged by a set

65 of detectors. Consequently, some signal is lost between cells of the imager, and the detectors are more expensive. On the other hand, the QMZ only needs four detectors, and each detector measures the entire signal at each output.

The second critical element is the UV laser system, which can be either diode-pumped and injection-seeded solid-state lasers (Lux et al., 2020) or microchip lasers amplified in free space (Wirth et al., 2009). This type of laser has the disadvantage of being sensitive to vibrations due to the number of free space optics and the presence of piezo-monitored optics to

70 maintain the laser cavity adapted to the injected wavelength. These challenges have led to significant developments for DELICAT Laser (similar to WALES (Wirth et al., 2009)) and AEOLUS laser (even though, in this case, the difficulty also involved the space environment (Mondin et al., 2017)). In this regard, fiber laser systems can lead to better performances for on-board direct detection wind lidar. Additionally, fiber lasers have the advantage of being robust to vibrations, lighter, and more cost-effective when commercialized.

75 The third critical aspect concerns the method applied to measure the vertical and lateral wind components. To reconstruct the two components of the wind vector, the typical method involves directing the lidar in four directions, making an angle θ with the flight trajectory, distributed around a circle. Typically, the lidar is pointed upward and downward to measure the vertical component and to the left and right to measure the lateral component (see Fig. 1). The two wind components are then derived from the four projections using a linear least squares method (Augere et al., 2016). This assumes

80 that the wind is homogeneous, so the projections measured on the different axes correspond to the same wind vector.

In the case of turbulence, the angle θ is generally chosen between 15° and 20° (Kikuchi et al., 2020) to satisfy the condition of a quasi-homogeneous wind field, as the measurement points are close to each other and, therefore, more correlated. However, the error committed in the reconstruction of the two wind components for small angles is given by $\frac{f(\delta V_p)}{2\tan\theta}$, where $f(\delta V_p)$ is a function depending on the error δV_p induced by turbulence on the projections. The factor $\frac{1}{2\tan\theta}$ can lead to
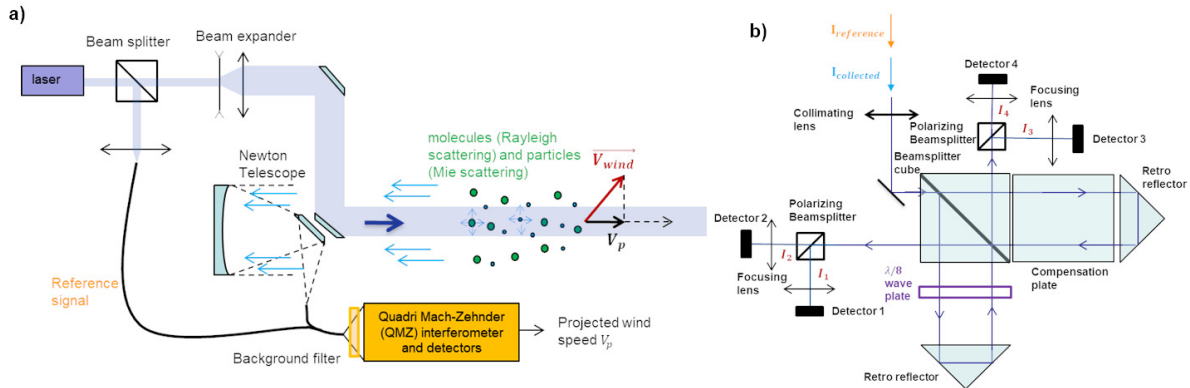
Figure 2. a) Schematic of the bistatic coaxial architecture chosen for the UV Doppler Wind lidar. b) Schematic of the Quadri Mach-Zehnder

significant error amplifications ($\approx 1,9 - 1,4$ for $\theta = 15° - 20°$). To our knowledge, none of the studies have optimized the angle to minimize the error in the reconstructed 3D wind in the case of turbulence.

In this article, we present a study in which we have optimized the architecture of a molecular lidar designed to measure the lateral and vertical wind in front of an aircraft for Gust Load Alleviation (GLA) applications, aiming to maximize its performance by minimizing the error in the reconstructed wind. The design includes a robust Quadri Mach-Zehnder (QMZ) interferometer, fiber laser architectures, and an optimization of the scanning angle. To optimize the lidar architecture, an end-to-end simulator was developed to determine the collected light, the signal-to-noise ratio on the detectors, and the calculation of the error in the wind measurement projected on the lidar axis for a QMZ spectral analyzer. This simulator was used to optimize the telescope architecture, the detectors, the solar filter, and the laser parameters. Specifically, we determined lidar performance based on laser parameters and derived designs for a solid-state laser, a fiber laser, and a fiber laser followed by free-space amplifiers (hybrid fiber laser). For the vertical and lateral wind reconstruction, we optimized a design where the lidar is directed along four directions (up, down, left, and right) to measure the three components of the wind vector. This involves minimizing the analytical calculations of the error in the estimation of the vertical and lateral wind components with the lidar angle. In the case of turbulence described by the Von Karman model, the error is minimized for an angle of about 50°. This improves the Root Mean Squared Error (RMSE) by about 50% compared to the typical design using an angle of 15°-20°. These results were confirmed by simulations of an aircraft traveling over 8 km through turbulence described by the Von Karman model.

2 Lidar architecture optimization

First, we present the architecture of the lidar and the robustified QMZ interferometer. Secondly, we present the simulator that was used for the optimization of the lidar. Thirdly, we utilize the simulator to optimize various components of the lidar, including the emission/reception telescope, the solar filter, the detectors, and the laser parameters.

2.1 Lidar architecture

The architecture of the direct detection UV Doppler wind lidar is shown in Fig. 2.a). The laser emits pulses at 355 nm for solid-state lasers and at 343 nm for fiber lasers. A beam splitter is inserted to take a sample of the laser, serving as a reference signal. The laser light passes through a beam expander that focuses the laser at long distances. A Newton
110 telescope is used to collect the signal backscattered by molecules and particles and focus it into a multimode fiber. The signal goes through a solar filter to greatly reduce the light coming from the background. A fiber coupler is used to combine the collected backscattered light and the reference signal. The long fiber is employed either on the reference signal or on the backscattered signal to temporally separate the two signals at the input of the interferometer. Both signals pass through a spectral analyzer. The intensities measured by the detectors are compared for the two signals to determine
115 $\delta\varphi$ and to deduce the projected wind speed. It should be noted that the reference signal also allows obtaining absolute synchronization of the measured signal.

The QMZ interferometer is shown in Fig. 2.b). The signal, coming from the multimode fiber, is collimated by a converging lens and passes through a 50/50 beam splitter cube, which splits the beam into two arms of different lengths. A $\lambda/8$ wave plate on the short arm increases the optical path difference (OPD) for horizontal polarization by $\lambda/4$ considering the round
120 trip, compared to vertical polarization. On the long arm, a glass plate is used to reduce beam divergence and improve the overlap of the two beams on the detector. This leads to an increase in the angular acceptance of the interferometer (Smith and Chu, 2016). The beams from both arms are combined on the 50/50 beam splitter cube. The OPD of the output that has undergone an odd number of reflections is shifted by $\lambda/2$ relative to the other. On each output, a polarizing beam splitter cube separates the horizontal and vertical polarizations. This gives four outputs with OPDs given by D_0, $D_0 + \lambda/4$, $D_0 + \lambda/2$
125 and $D_0 + 3\lambda/4$ for I_1, I_2, I_3 and I_4, respectively. These outputs are focused on detectors that convert optical signals into current. The current is converted to voltage, which is then sampled and digitized into a computer. Signal processing makes it possible to recover the phase of the interference, the frequency offset, and finally the projected wind speed.

We have chosen an architecture that includes one 50/50 beam splitter cube for the separation and recombination of the beams, along with two retroreflectors forming the two arms, to create a robust interferometer. Indeed, the QMZ is not
130 sensitive to angular misalignment. However, simulations (Boulant et al.) show that lateral beam shift needs to be positioned within 2 µm. This is achieved using an X,Y mount on one retroreflector.

2.2 UV lidar simulator

A simulator has been developed to optimize the lidar architecture for the GLA application. It comprises three steps. The first step calculates the emission/reception overlap function to determine the number of backscattered photons. The second
135 step assesses the signal-to-noise ratio at the outputs of the detectors, and the third step determines the standard deviation of the wind speed to evaluate the overall lidar performance.

To calculate the overlap function, we use the method presented in the thesis manuscript of [Cezard (2008) (part 3.2.)] and [(Liméry, 2018) (part 3.3.4)]. The simulator first computes the laser propagation using the Gaussian beam approximation.

For each point along the laser beam, described by a distance from the telescope and the laser axis (assuming cylindrical symmetry), the simulator determines the image of the point by the first pupil and the amount of light that enters the fiber. Subsequently, for each distance from the telescope, the simulator integrates all the quantities obtained with all the points of the laser beam to calculate the ratio of the light that enters the fiber to the light collected by the pupil. The configuration is optimized for a given distance when the overlap function is equal to one.

Secondly, the simulator calculates the total signal-to-noise ratio (SNR), which is the collected light integrated over a range gate to the square root of the quadratic sum of all noise. To calculate the signal, we use the molecular backscattering and absorption coefficients determined with the evolution of the molecular density calculated using the US standard atmosphere model (Atmosphere, 1976). Particle backscattering is neglected at high altitudes because the concentration of particles is very low, leading to a backscattering much lower than the molecular backscattering. Then, the previously determined overlap function is used to calculate the collected signal. The total noise corresponds to the quadratic sum of the shot noise of the backscattered signal, the background noise, the speckle noise of the backscattered signal, and the detection noise, which includes the dark noise of the detector and the electronic noise (Fujii and Fukuchi, 2005, p. 488, 574 and 695). The configuration is considered optimized for a given average laser power (roughly proportional to the laser volume) when the noise is limited by the shot noise of the backscattered signal. Indeed when this noise dominates, the total SNR during the measurement time is proportional to $\sqrt{N * PRF}$ with N the number of backscattered photons and PRF the pulse repetition frequency. As N depends on the laser energy E_p, the SNR can only be improved by increasing the average power of the laser Pmoy = $E_p * PRF$.

The third step of the simulator is dedicated to calculating the standard deviation of the wind speed for the total SNR in order to assess the measurement performance. For simplicity, we utilized the analytical formula derived by Bruneau and Pelon (2003) and incorporated the contribution of speckle noise into this formula. The calculation details are outlined in Appendix A. We verified that this formula was a good estimator using Monte Carlo simulations. In these simulations, we stochastically generated the currents obtained at the detector outputs based on the statistics of the various noise sources. Subsequently, the four currents were convolved with the detector impulse response. The Maximum Likelihood Estimator (MLE) was then employed to reconstruct the wind profile along the laser axis, and we assessed the error distribution across multiple simulations. Furthermore, we confirmed that the results obtained using the analytical formula closely matched Cramer Rao's lower bound.

2.3 Optimization of the lidar performances

2.3.1 Emission/reception architecture

Several simulations were conducted to determine the optimal focusing distances for both the telescope and the laser, aiming to maximize the overlap function between 100 m and 300 m for our optical architecture. The setup includes a telescope with a diameter of 152.4 mm, a primary mirror focal length of 609.6 mm, a second mirror obstruction diameter of 38 mm, and a fiber diameter of 400 μm. These calculations were performed considering a laser beam with a size of 36

mm upon exiting the lidar, where $M^2 < 8$. The optimized focusing distances were found to be 155 m for the telescope and 100 m for the laser, resulting in an overlap function equal to 1 across the entire range.

2.3.2 Detector

175 We compared the detection noise level in terms of the number of photons for the specified range gate across three types of detectors: a PIN photodiode amplified with a transimpedance, an avalanche photodiode (APD), and a PMT (Hamamatsu S5971; Hamamatsu S9075; Hamamatsu R10721-210). Indeed, the total noise induced by the backscattered shot noise must exceed the total detection noise. This leads to the condition $N >> \frac{4\sigma_{det}^2}{G^2F\eta}$, where N represents the sum of backscattered photons obtained from the four detectors, σ_{det}^2 denotes the detection noise of a detector expressed in the number of electrons calculated for a range gate of 25 m, G stands for the gain of the detector, F represents the excess noise factor, and 180 η signifies the quantum efficiency. For the PIN, we found $4.2 \times 10^6 N_{photons}$, for the APD $1.7 \times 10^5 N_{photons}$, and for the PMT $1.23 \times 10^{-6} N_{photons}$. Only the PMT ensures a low level of detection noise compared to the shot noise level.

2.3.3 Solar filter

The thin solar filter blocks most of the background signal (broad spectrum) that goes to the spectral analyzer but transmits 185 the Rayleigh signal. Ideally, the filter bandwidth should encompass the spectral width of the Rayleigh signal plus and minus the maximum Doppler frequency shift (≈1 pm at 355 nm for a wind speed of 100 m/s). However, the smaller the desired filter bandwidth, the smaller the transmission and the more expensive the component.

To optimize the filter, we need $\frac{N}{N_{bkg}} > 10$ where N_{bkg} is the sum of background photons of the four detectors. This lead to:

$$E_P > BR\Delta\lambda r^2 \tag{1}$$

190 where $B = \frac{10\pi FOV^2}{c\beta T_{atm}^2 \gamma(r)2}$, R is the background radiance, r the range to the telescope, c the celerity of light, β the backscatter coefficient, T_{atm} the atmospheric transmission, FOV is the telescope field of view and Δλ is the filter bandwidth. We can see that the optimized filter depends on the laser parameters.

As the minimum energy of the pulse increases with distance, in our case Eq. 1 must be fulfilled at 300 m to be fulfilled over the whole range. We also assume for the study a background radiance taken equal to 0,3 W/m^2/sr/nm. For a filter 195 bandwidth of 1 nm, this results in a minimum laser energy per pulse of $E_{pmin} = 88\mu J$.

2.3.4 Laser optimization on the ground and at 10 km of altitude

To optimize the laser parameters using the simulator, simulations were performed by adjusting the average laser power and pulse repetition frequency to assess the error in the retrieved wind velocity. We assumed a 1 nm solar filter with a transmission of 1 and neglected electrical noise by considering PMT detectors. At low altitudes (less than 1 km), we assumed 200 a backscatter coefficient for particles of $1.10^{-7} m^{-1}.sr^{-1}$. The simulations were performed at a distance of 150 m in front of the aircraft, which corresponds to the intended measurement distance. Additionally, we assumed a range gate of 25 m
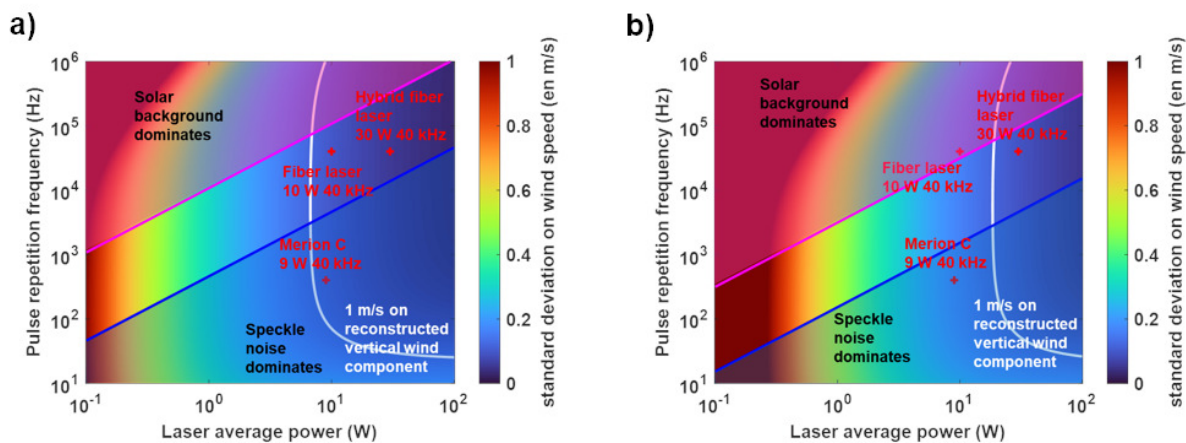
Figure 3. a) Standard deviation on wind speed estimation as a function of laser average power and pulse repetition frequency at 300m from the lidar, at 0 km considering molecular scattering and particles scattering. The white line shows the limit of 1 m/s on the reconstructed vertical wind component. b) Standard deviation on wind speed estimation as a function of laser average power and pulse repetition frequency at 180m from the lidar, at 10 km altitude with pure molecular backscattering

to match the GLA specifications. The measurement times were set to 0.1 s, corresponding to an integration over 25 m for an aircraft traveling at 250 m/s. We considered that the laser has a spectral width of <500 MHz, significantly less than the spectral broadening induced by the thermal movement of the molecules (3 GHz). Therefore, only the molecular spectral

205 broadening was taken into account in the calculations. The simulations were conducted both on the ground and at 10 km altitude, approximately corresponding to the aircraft's cruising altitude, as the GLA must operate throughout the flight.

Figure 3.a) shows the evolution of the standard deviation of the projected wind speed computed on the ground. The white line gives the laser parameters resulting in an error, equivalent to 3σ (where σ denotes the standard deviation), of 1 m/s on the reconstructed vertical wind component for a scanning angle of 15°. The methodology utilized for wind

210 calculation is elaborated in section (3.1). This error corresponds to 0.27 m/s on the projected wind speed. The magenta line denotes the threshold where the shot noise of the backscattered signal exceeds ten times the background noise at 300 m. Beyond this threshold, the laser pulse energy diminishes, leading to an increased number of background photons compared to backscattered photons. The blue line represents the boundary where the shot noise of the backscattered signal surpasses ten times the speckle noise of the backscattered signal at 100 m. Below this threshold, averaging the mea-

215 surements fails to adequately average speckle patterns. Within the region delineated by these lines, the measurement is constrained by the shot noise of the backscatter, and the lidar is considered optimized. Within this range, performance is directly proportional to the average laser power (laser parameter serving as an indicator of laser size).

Figure 3.b) shows the evolution of the standard deviation of the wind speed computed at 10 km altitude, featuring the same threshold lines as in Fig. 3.a). Performance is diminished, and achieving an accuracy of 1 m/s is more challenging

220 at this altitude. This difficulty arises from the absence of particles and the reduced density of molecules at this altitude,

resulting in a decreased amount of backscattered signal. Additionally, the scarcity of signal amplifies the impact of the background signal, as evidenced by the magenta line being lower than that calculated on the ground. Conversely, the speckle noise decreases because the backscattering is predominantly molecular, which is less coherent than particulate backscattering.

2.3.5 Selected laser configurations

We have used the Fig. 3 to select laser parameters for three laser technologies: seeded solid states laser, fiber laser and hybrid fiber laser.

Regarding the seeded solid-state laser, the primary challenge lies in achieving a high repetition rate to avoid being constrained by speckle noise. We have opted for the injection-seeded Merion C commercialised by Lumibird, which boasts a repetition rate of 400 Hz and delivers 22.5 mJ of energy per pulse. In this scenario, a wide bandwidth solar filter can be employed (typically >> 10 nm is chosen). This configuration yields a standard deviation σ_{lidar} of 0.11 m/s at low altitude and 0.18 m/s at high altitude.

The second technology is a fiber laser, made with doped and pumped fiber, emitting at 1 µm, with a frequency tripling stage. Because of the limit in peak power due to the Brillouin effect in the fiber, we chose a high repetition rate of 40 kHz well adapted to the fiber laser. We estimated that the maximum average power of 10 W can be achieved with current technology, it allows the use of a solar filter up to 11 nm. The results for standard deviation σ_{lidar} are 0,10 m/s at low altitude and 0,17 m/s at high altitude.

The third configuration is the hybrid fiber laser, obtained by adding a free space amplifier at the output of the fiber laser. We estimated that the maximum average power of 30 W can be reach, which allows the use of a solar filter up to 33 nm. This results in a standard deviation σ_{lidar} of 0,06 m/s at low altitude and 0,09 m/s at high altitude.

3 Wind reconstruction

We minimized the total error in the vertical and lateral components of the wind reconstructed using the four-axis design in the presence of turbulence. These components significantly influence lift, emphasizing the importance of accurate estimation to avoid errors when attenuating the tubrulence effect in GLA applications. Firstly, we establish the expression of the instrumental error contribution to the total error and evaluate it for the three laser designs previously established. Secondly, we define the expression of the turbulence contribution to the total error for Von Karman turbulence. Thirdly, we determine the lidar angle that minimizes the total error in the vertical component.

3.1 Lidar angle optimization with analytical method

The first step involves establishing the contribution of instrumental error to the total error in the vertical and lateral wind components, which depends on the error in the projections used to estimate the vertical component and the lidar angle. Referring to Figure 1, the vertical wind component is given by $v_z = \frac{V_3 - V_1}{2\sin(\theta)}$, where V_3 and V_1 are projections
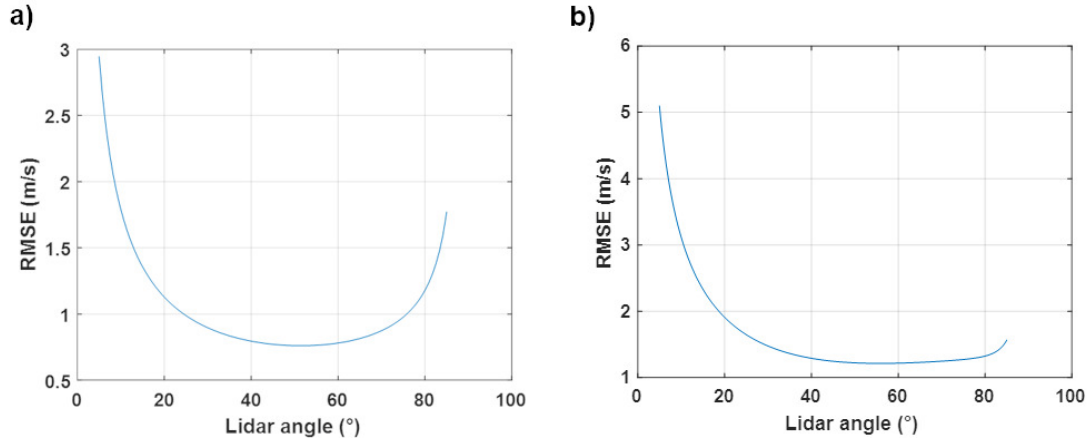
Figure 4. a) Root mean squared error between the reconstructed and actual lateral component on the flight path as a function of the lidar angle from the flight direction θ, for wind measurement at high altitude. b) Root mean squared error between the reconstructed and actual lateral component on the flight path as a function of the lidar angle from the flight direction θ, for wind measurement at low altitude

of the wind onto axes 3 and 1, respectively. The lateral component is reconstructed using the same formula, employing projections from axes 2 and 4, V_2 and V_4. These projections are affected by the lidar noise σ_{lidar}, evaluated in section 2.3.5 for the three laser designs. Thus, the error in the vertical wind component due to instrumental noise is given by

$\sigma_{Vz,instrumentale}(d,\theta) = \frac{\sqrt{2}}{(2\sin(\theta))}\sigma_{lidar}(d,\theta)$. The error in the lateral component is the same due to symmetry. This error depends on d, the range of estimation along the flight path, and θ since σ_{lidar} depends on the range z from the lidar, where z = d/cos θ. Moreover, if we suppose that the lidar is optimized, which is the case for the hybrid fiber laser between 100 m and 300 m, the predominant noise is the backscattered signal shot noise. In this scenario, σ_{lidar} is proportional to the measurement range z along the lidar axis. Given that the standard deviation for the three laser configurations was calculated at $z_0 = 150$ m, the instrumental noise at range d is $\sigma_{lidar}(d,\theta) = \frac{\sigma_{lidar}(z_0)}{z_0}\frac{d}{\cos(\theta)}$. Therefore, the instrumental error contribution to the total error in the vertical wind component is:

$$\sigma_{Vz,instrumentale}(d,\theta) = \frac{\sqrt{2}}{(2sin(\theta))}\frac{\sigma_{lidar}(z_0)}{z_0}\frac{d}{cos(\theta)} \tag{2}$$

We assess the error in the reconstructed vertical and lateral wind components for the three selected laser configurations. Assuming an estimation distance of d = 100 m and an angle of 15°, typically used for the scan angle, we obtain errors of 0.33 m/s, 0.32 m/s, and 0.18 m/s for the Merion C laser, the fiber laser, and the hybrid fiber laser, respectively. This result ensures that the 3 σ error for all three designs remains below 1 m/s.

The second step involves establishing the expression of the turbulence contribution to the total error for turbulence described by the Von Karman model. This model provides expressions for power spectral densities that best match measured turbulence data (Giez et al., 2021), particularly in the inertial subrange where the energy cascade from large eddies

270 to smaller ones occurs. The error in the vertical wind component, corresponding to the root mean square error between the reconstructed component and the actual component, if we only consider the turbulence contribution, is:

$$\sigma_{Vz,turbulence}(d,\theta) = \sqrt{\langle (V_z - V_{z0})^2 \rangle}$$

$$= \sqrt{\frac{2}{(2sin(\theta))^2}(\langle \delta V_{p1}^2 \rangle + \langle \delta V_{p3}^2 \rangle - 2\langle \delta V_{p1} \delta V_{p3} \rangle)} \tag{3}$$

where V_{z0} is the vertical component of the actual wind, δV_{p1} and δV_{p3} are the differences between the projections of the
275 real wind and the measured projections, for axis 1 and 3 respectively (see Fig. 1). The symbols $\langle \rangle$ account for the ensemble averaging. For a Von Karman turbulence, that is homogeneous and isotropic (i.e. the statistics are independent of the coordinate rotations), the error is (calculation details in appendix B, using the formulas presented in (Wilson, 1998)):

$$\sigma_{Vz,turbulence}(d,\theta) = \sqrt{\frac{D_{NN}(2r)}{(2tan(\theta))^2} + \frac{3B_{LL}(0) + B_{LL}(2r)}{2} - 2B_{LL}(r)} \tag{4}$$

where $r = d\tan(\theta)$ is the distance between the point on the lidar axis and the point on the flight path, B_{LL} the longitudi-
280 nal correlation function of the turbulence (for the wind component longitudinal to the displacement vector r) and D_{NN} the structure function for the lateral component of the wind (lateral to the displacement vector r). Combining equations (52),(99) and (101) of (Wilson, 1998), we obtain expressions for the correlation and structure functions:

$$B_{LL}(r) = \sigma^2 \frac{2}{\Gamma(1/3)}(\frac{r}{2l})^{1/3}K_{1/3}(\frac{r}{l}) \tag{5}$$

$$B_{NN}(r) = \sigma^2 \frac{2}{\Gamma(1/3)}(\frac{r}{2l})^{1/3}[K_{1/3}(\frac{r}{l}) - (\frac{r}{2l})K_{2/3}(\frac{r}{l})] \tag{6}$$

285 $$D_{NN}(r) = 2(B_{NN}(0) - B_{NN}(r)) \tag{7}$$

where σ^2 is the variance of the turbulence, l the turbulence length scale, Γ is the gamma function, K_n is a Bessel function of the first kind and B_{NN} the lateral correlation function of the turbulence.

The optimization of the lidar angle was performed by minimizing the expression of the total error on the vertical wind component with respect to θ. The expression for the total error is $\sigma_{Vz} = \sqrt{\sigma_{Vz,instrumentale}(d,\theta)^2 + \sigma_{Vz,turbulence}(d,\theta)^2}$. This
290 error was evaluated for a range of estimation of $d = 100$ m at an altitude of 10 km, using the Merion C laser, and a Von Karman turbulence with l equal to 762 m (2000 feet) and σ^2 equal to 1 $(m/s)^2$. Figure 4.a) illustrates the evolution of the total error, noted RMSE for root mean square error between the reconstructed and actual lateral component along the flight path, as a function of the scan angle θ. The RMSE reaches a minimum for a scanning angle of 51°. The RMSE obtained for this angle is 0.76 m/s, nearly twice as low as the RMSE of 1.35 m/s obtained for an angle of 15°. Choosing an angle of 51° may
295 seem counter-intuitive, as the measurement points are much further apart for such an angle (2r = 240 m between the two opposite points for 50°, while 2r = 36 m for 15°). Due to this larger distance, one might assume that the measurement points are not correlated, leading to significant errors in the projections, which affect the reconstructed wind component. In fact, for the wind structure we are examining (in the inertial subrange), in a turbulent wind field like Von Karman turbulence, large eddies are much more influential than small ones. The smaller wind structures induce only a minor error on all

300   four projections, which can be amplified for small scanning angles due to the factor $1/(2\sin(\theta))^2$ when retrieving the wind component. For larger angles (above 50°), the instrumental noise becomes significant because the measurement range along the lidar axis increases.

3.2   Optimized angle for measurements at low altitude

We study the evolution of the optimized angle for measurement on the ground. The measurement parameters remain the
305   same: the vertical wind component is estimated at $d = 100$ m from the lidar using the Merion C laser. The length scale of the Von Karman turbulence at low altitude is much lower and is assumed to be equal to 100 m for this study. Additionally, we assume a turbulence strength σ^2 of 1 $(m/s)^2$. The evolution of the RMSE at this altitude is depicted in Figure 4.b) as a function of the lidar angle. We observe that the optimized angle is around 55°. However, the error is higher than at high altitude, partly due to the fact that smaller eddies have more energy. This increases the difference between the projections
310   of the real wind and the measured projections, thereby increasing the error.

3.3   Validation with simulations of turbulence at 10 km of altitude

To illustrate the improvement at 50°, reconstruction simulations of the lateral wind component with two scanning angles were conducted. The simulation utilized a simulator that calculates the 3D wind field by following the statistics of the Von Karman turbulence model, using the equations presented in the Army Research Laboratory technical report (Wilson, 1998).
315   The 3D spectra are calculated as a function of the spatial frequency: $\Phi_{ij}(k) = \frac{E_v(k)}{4\pi k^4}(\delta_{ij}k^2 - k_i k_j)$ where the indices i and j represent the direction (x, y, or z), k represents the spatial frequency, $E_v(k)$ is the spectrum energy of turbulence, and δ_{ij} is the Kronecker delta. For Von Karman turbulence, $E_v(k) = 1.4528\frac{\sigma^2 k^4 L_0^5}{(1+k^2 L_0^2)^{17/6}}$, where σ^2 denotes the variance of turbulence. For each k, a 3 by 3 symmetric matrix $M(k) = (\Phi_{ij}(k))_{i=[x,y,z],j=[x,y,z]}$ is obtained, which is factorized using a Cholesky decomposition to facilitate the generation of correlated random wind. This matrix is then multiplied by a vector of 3 random phases
320   following a reduced centered normal distribution for each k. The three correlated wind components are obtained with an inverse Fourier transformation according to k. Note that the temporal evolution of the wind is not taken into account to simplify the study, assuming that the wind does not vary significantly as the plane moves through the grid. Once the winds are simulated, the plane traverses the grid with the lidar in the nose, and the wind is reconstructed in front of it with the same measurement geometry as before.
325   Figure 5) displays the results. In Fig. 5.a), an example of wind simulated according to the Von Karman model is depicted. In Fig. 5.b), the green line, which corresponds to the vertical component retrieved with a scanning angle of 50°, closely matches the black line (representing the real wind) compared to the red line, which corresponds to the vertical component recovered with an angle of 15°. This illustrates the improvement achieved with the optimized scanning angle of 50°.
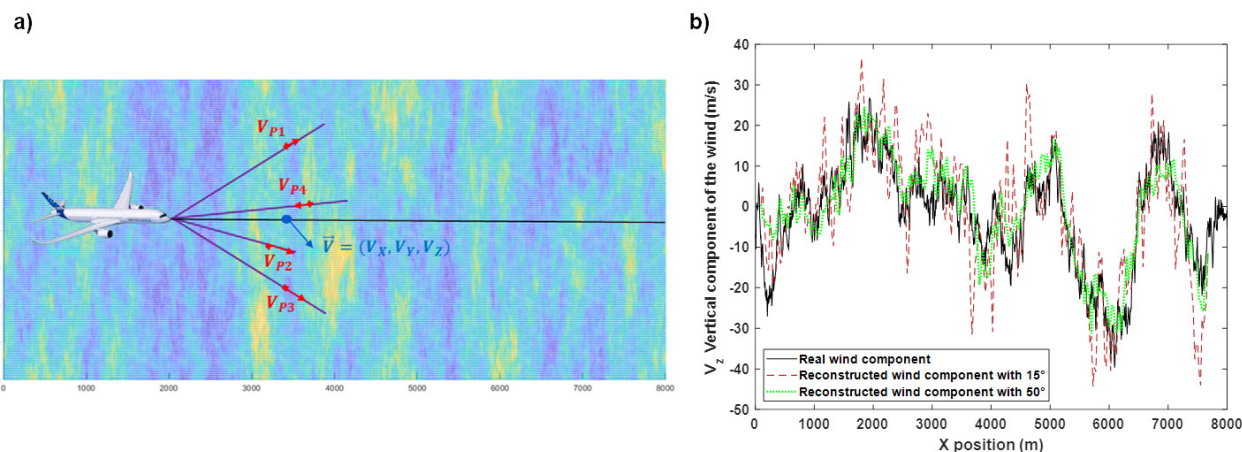
Figure 5. a) Sample of a wind simulation (norm of the wind vector, in the plan xOz) and representation of the lidar measurements for the wind reconstruction ahead of a plane b) Evolution of the vertical wind component as a function of the position in the simulated wind volume. In black the actual wind component on the flight path, in red the wind component retrieved with an angle of 15°, in green with an angle of 50 °

4   Conclusions

330   A robust UV lidar architecture, including a QMZ interferometer and a fiber laser, was presented for measuring wind in the feed-forward GLA system. The end-to-end simulator of the lidar was described and utilized to optimize its architecture. The transmitter/receiver configuration was optimized to ensure complete overlap of the laser and telescope field of view between 100 m and 300 m. PMTs were chosen due to their high gain, which helps limit the impact of detection noise. An optimized solar filter size was estimated for each laser configuration to mitigate the background signal. Three lasers were

335   selected: a commercial laser, the Merion C, for initial testing, and two fiber laser models studied at ONERA. The error on the projected wind speed estimated at 150 m on the laser axis are 0.175 m/s for the Merion C, 0.167 m/s for the fiber laser, and 0.094 m/s for the hybrid fiber laser.

A lidar angle optimization method was presented. This method evaluates the RMSE between the reconstructed vertical wind component and the actual one on the flight path for a linear least squares method. Two contributions are considered,

340   instrumental noise and noise induced by turbulence. The angle that minimizes the RMSE in the presence of Von Karman turbulence is approximately 50°, resulting in an RMSE that is approximately 50% of the RMSE obtained with an angle of 15°-20°. The method has been validated through simulations of turbulence and wind reconstruction. It should be noted that this method can also be applied by considering only instrumental noise. Additionally, this method demonstrates that the intuition of using a small lidar angle to maintain almost homogeneous wind field conditions between measurement

345   points to minimize error on the vertical component is incorrect for Von Karman turbulence.

To be noted that further reconstruction method are studied at ONERA to decrease the error on the reconstructed wind speed.

Appendix A: Lidar measurement standard deviation with Speckle noise

A1   estimation of the projected wind speed from the four currents

350   At the output of the four detectors, if we assume that there is the same transmision at the four outputs of the QMZ and the interferometer introduces no loss of contrast, the signals in current are :

$$S_1 = \frac{S_0}{4}(1 + M_{tot}cos(\varphi)) + S_{bkg} + S_{dark} \tag{A1}$$

$$S_2 = \frac{S_0}{4}(1 - M_{tot}sin(\varphi)) + S_{bkg} + S_{dark} \tag{A2}$$

$$S_3 = \frac{S_0}{4}(1 - M_{tot}cos(\varphi)) + S_{bkg} + S_{dark} \tag{A3}$$

355    $$S_4 = \frac{S_0}{4}(1 + M_{tot}sin(\varphi)) + S_{bkg} + S_{dark} \tag{A4}$$

where S_0 the total current, M_{tot} the contrast of the interferences due to the spectral shape of the input light, S_{bkg} the signal due to the background signal, S_{dark} the noise from the detector and φ a simpler notation of $\delta\varphi_{OPD}$. The spectrum of the incident light is from two scattering process, Rayleigh scattering and Mie scattering, so $M_{tot} = \frac{1}{R_\beta}M_m + \frac{R_\beta - 1}{R_\beta}M_p$ with R_β is the backscatter ratio, M_m the interference contrast due to the Rayleigh spectrum and M_p the interference contrast due to

360   the Mie spectrum.

Considering that the background noise and the detection noise can be estimated and subtracted to the signals, φ can be estimated by :

$$Q_1 = \frac{S_1' - S_3'}{S_1' + S_3'} = M_{tot}cos(\varphi) \tag{A5}$$

$$Q_2 = \frac{S_4' - S_2'}{S_4' + S_2'} = M_{tot}sin(\varphi) \tag{A6}$$

365    $$\varphi = Arctan(\frac{Q_2}{Q_1}) \tag{A7}$$

where S_i' indicates that background noise and the detection noise have been subtracted to the signals S_i. Doing the same with the reference signal (i.e the laser light), we obtain φ_0 and the projected wind speed is estimated with:

$$v_p = \frac{\lambda_0 c}{4\pi\Delta L}(\varphi - \varphi_0) \tag{A8}$$

A2   standard deviation on the wind speed due to the Speckle noise

370   Let's note $Q = \frac{Q_1}{Q_2}$ and $S_\varphi = \frac{4\pi\Delta L}{\lambda_0 c}$. The standard deviation of v_p is (neglecting the standard deviation on φ_0 because the reference signal is sufficiently high to have a good SNR):

$$\sigma_{v_p} = \frac{1}{S_\varphi}\sigma_\varphi \tag{A9}$$

where σ_φ is the standard deviation on φ :

$$\varphi = \frac{d\varphi}{dQ}\sigma_Q = \cos\varphi^2\sigma_Q \tag{A10}$$

375   with σ_Q the standard deviation on Q. The variance on Q is (as Q_1 end Q_1 are uncorrelated):

$$var(Q) = Q^2\left(\frac{var(Q_1)}{Q_1^2} + \frac{var(Q_2)}{Q_2^2}\right) \tag{A11}$$

Taking the expression (A5) we have :

$$var(Q_1) = Q_1^2\left(\frac{var(S_1' - S_3')}{(S_1' - S_3')^2} + \frac{var(S_1' + S_3')}{(S_1' + S_3')^2} - 2\frac{cov(S_1' - S_3', S_1' + S_3')}{(S_1' - S_3')(S_1' + S_3')}\right) \tag{A12}$$

Assuming that S_1' and S_3' are uncorrelated, we have:

380   $$var(S_1' - S_3') = var(S_1' + S_3') = var(S_1') + var(S_3') \tag{A13}$$

$$cov(S_1' - S_3', S_1' + S_3') = var(S_1') - var(S_3') \tag{A14}$$

The variance of Q_1 is:

$$var(Q_1) = (1 + Q_1^2)\frac{var(S_1') + var(S_3')}{(S_1' + S_3')^2} - 2Q_1\frac{var(S_1') - var(S_3')}{(S_1' + S_3')^2} \tag{A15}$$

In the case where the Speckle noise dominates we have $var(S_1') = \frac{S_{1m}'^2}{N_m} + \frac{S_{1p}'^2}{N_p}$ with $S_{1m} = \frac{S_{0m}}{4}(1 + M_m\cos(\varphi))$ and $S_{1p} = \frac{S_{0p}}{4}(1 + M_p\cos(\varphi))$

385   where S_{0m} and S_{0p} are the intensities at the input of the interferometer coming from molecules and particle respectively. Same thing for $var(S_3') = \frac{S_{3m}'^2}{N_m} + \frac{S_{3p}'^2}{N_p}$ with $S_{3m} = \frac{S_{0m}}{4}(1 - M_m\cos(\varphi))$ and $S_{3p} = \frac{S_{0p}}{4}(1 - M_p\cos(\varphi))$. Then:

$$var(Q_1) = (1 + Q_1^2)\frac{\frac{(S_{0m}/4)^2}{N_m}(2 + 2M_m^2\cos(\varphi)^2) + \frac{(S_{0p}/4)^2}{N_p}(2 + 2M_p^2\cos(\varphi)^2)}{(S_0/2)^2} - 2Q_1\frac{\frac{(S_{0m}/4)^2}{N_m}4M_m\cos(\varphi) + \frac{(S_{0p}/4)^2}{N_p}4M_p\cos(\varphi)}{(S_0/2)^2} \tag{A16}$$

We can see that two contributions appear in the expression: the one from the Rayleigh signal and the one of the Mie signal. In the following, we only made the calculation for the Rayleigh signal and consider that the calculation are the same for the

390   Mie signal. If we note $Q_{1m} = M_m\cos(\varphi)$ and $Q_{1p} = M_p\cos(\varphi)$, the variance of Q_1 is:

$$var(Q_1) = \frac{\frac{(S_{0m}/4)^2}{N_m}(2 + 2Q_{1m}^2) + \frac{(S_{0m}/4)^2}{N_m}(2Q_1^2 + 2Q_1^2Q_{1m}^2) - 8Q_1Q_{1m}\frac{(S_{0m}/4)^2}{N_m} + \text{(Mie part)}}{(S_0/2)^2}$$

$$= \left(\frac{S_{0m}}{S_0}\right)^2\frac{1}{2N_m}[(1 - Q_1Q_{1m})^2 + (Q_1 - Q_{1m})^2] + \left(\frac{S_{0p}}{S_0}\right)^2\frac{1}{2N_p}[(1 - Q_1Q_{1p})^2 + (Q_1 - Q_{1p})^2] \tag{A17}$$

For the variance of Q_2, the calculation is the same:

$$var(Q_2) = (\frac{S_{0m}}{S_0})^2 \frac{1}{2N_m}[(1-Q_2Q_{2m})^2 + (Q_2 - Q_{2m})^2] + (\frac{S_{0p}}{S_0})^2 \frac{1}{2N_p}[(1-Q_2Q_{2p})^2 + (Q_2 - Q_{2p})^2] \qquad (A18)$$

395   with $Q_{2m} = M_m sin(\varphi)$ and $Q_{2p} = M_p sin(\varphi)$. Considering that the calculation are the same for the Rayleigh part and the Mie part of the formula, we have:

$$\frac{var(Q_1)}{Q_1^2} + \frac{var(Q_2)}{Q_2^2} = (\frac{S_{0m}}{S_0})^2 \frac{1}{2N_m}[\frac{(1-Q_1Q_{1m})^2 + (Q_1-Q_{1m})^2}{Q_1^2} + \frac{(1-Q_2Q_{2m})^2 + (Q_2-Q_{2m})^2}{Q_2^2}] + \text{(Mie part)}$$

$$= (\frac{S_{0m}}{S_0})^2 \frac{1}{2N_m} \frac{M_{tot}^2[1 + (M_{tot}^2 M_m^2 - 4M_{tot}M_m + 2(M_{tot}-M_m)^2)\frac{sin(2\varphi)^2}{4}]}{M_{tot}^4 cos(\varphi)^2 sin(\varphi)^2} + \text{(Mie part)} \qquad (A19)$$

Finally, the variance of Q is :

400
$$var(Q) = (\frac{S_{0m}}{S_0})^2 \frac{1}{2N_m M_{tot}^2 cos(\varphi)^2}[1 + (M_{tot}^2 M_m^2 - 4M_{tot}M_m + 2(M_{tot}-M_m)^2)\frac{sin(2\varphi)^2}{4}]$$

$$+ (\frac{S_{0p}}{S_0})^2 \frac{1}{2N_p M_{tot}^2 cos(\varphi)^2}[1 + (M_{tot}^2 M_p^2 - 4M_{tot}M_p + 2(M_{tot}-M_p)^2)\frac{sin(2\varphi)^2}{4}] \qquad (A20)$$

If we assume that atmospheric transmission are almost equal to 1, $\frac{S_{0m}}{S_0} \approx \frac{1}{R_\beta}$ and $\frac{S_{0p}}{S_0} \approx \frac{R_\beta - 1}{R_\beta}$. The variance on the projected wind due to the Speckle noise is:

$$\sigma_{v_p}^2 = (\frac{1}{R_\beta})^2 \frac{1}{2N_m M_{tot}^2 S_\varphi^2}[1 + (M_{tot}^2 M_m^2 - 4M_{tot}M_m + 2(M_{tot}-M_m)^2)\frac{sin(2\varphi)^2}{4}]$$

405
$$+ (\frac{R_\beta - 1}{R_\beta})^2 \frac{1}{2N_p M_{tot}^2 S_\varphi^2}[1 + (M_{tot}^2 M_p^2 - 4M_{tot}M_p + 2(M_{tot}-M_p)^2)\frac{sin(2\varphi)^2}{4}] \qquad (A21)$$

Appendix B: Expression of the MSE due to the turbulence

For the different wind, we will note $\mathbf{V} = (V_x, V_y, V_z)$ the wind on the flight path at range d, $\mathbf{V_1} = (V_{x1}, V_{y1}, V_{z1})$ the wind located at the measurement point of axis 1 and $\mathbf{V_3} = (V_{x3}, V_{y3}, V_{z3})$ the wind located at the measurement point of axis 3. Then $\delta V_{p1} = (V_{x1} - V_x)cos(\theta) - (V_{z1} - V_z)sin(\theta)$ and $\delta V_{p3} = (V_{x3} - V_x)cos(\theta) + (V_{z3} - V_z)sin(\theta)$. The variance of δV_{p1} is :

410   $$\langle \delta V_{p1}^2 \rangle = \langle (V_{x1}-V_x)^2 \rangle cos(\theta)^2 + \langle (V_{z1}-V_z)^2 \rangle sin(\theta)^2 - 2sin(\theta)cos(\theta)\langle (V_{x1}-V_x)(V_{z1}-V_z) \rangle \qquad (B1)$$

$\langle (V_{x1}-V_x)^2 \rangle$ and $\langle (V_{z1}-V_z)^2 \rangle$ correspond to the lateral structure function and longitudinal structure function respectively. The paper of Wilson (1998) gives the formula for the correlation between two wind component : $\langle V_i V_j \rangle(r) = (B_{LL}(r) - B_{NN}(r))\frac{r_i r_j}{r^2} + B_{NN}(r)\delta_{ij}$ with δ_{ij} the Kronecker symbol, r_i and r_j the components i and j of the displacement vector $\mathbf{r}$. As $r_x = 0$, the correlation between two wind components of different directions with one of them equal to x direction is equal to 0, that led to:

415

$$\langle \delta V_{p1}^2 \rangle = D_{NN}(r)cos(\theta)^2 + D_{LL}(r)sin(\theta)^2 \qquad (B2)$$

with $D_{LL}(r) = 2(B_{LL}(0) - B_{LL}(r))$. By symmetry, $\langle \delta V_{p1}^2 \rangle = \langle \delta V_{p3}^2 \rangle$. For the correlation between the two differences, we have :

$$\langle \delta V_{p1} \delta V_{p3} \rangle = \langle ((V_{x1} - V_x)cos(\theta) - (V_{z1} - V_z)sin(\theta))((V_{x3} - V_x)cos(\theta) + (V_{z3} - V_z)sin(\theta)) \rangle$$

$$= cos(\theta)^2 \langle (V_{x1} - V_x)(V_{x3} - V_x) \rangle - sin(\theta)^2 \langle (V_{z1} - V_z)(V_{z3} - V_z) \rangle$$

$$= cos(\theta)^2 (B_{NN}(2r) + D_{NN}(r) - B_{NN}(0)) - sin(\theta)^2 (B_{LL}(2r) + D_{LL}(r) - B_{LL}(0)) \tag{B3}$$

Here again, passage from B3 to B4 is due to the correlation between two wind components of different directions with one of them equal to x direction is equal to 0. Using equations B1 and B5 in the expression of $MSE_T|_{turbulence}$, we obtain :

$$MSE_T|_{turbulence} = \frac{2}{(2sin(\theta))^2} (\langle \delta V_{p1}^2 \rangle + \langle \delta V_{p3}^2 \rangle - 2\langle \delta V_{p1} \delta V_{p3} \rangle)$$

$$= \frac{D_{NN}(2r)}{(2tan(\theta))^2} + \frac{3B_{LL}(0) + B_{LL}(2r)}{2} - 2B_{LL}(r) \tag{B4}$$

$$\tag{B5}$$

Author contributions. Authors equally contributed to the writing of this paper

Competing interests. The authors declare that their is no competing interests

Acknowledgements. The authors wish to acknowledge Nicolas Cézard and Anasthase Liméry from ONERA for their help to the development of the simulation code of the emission/reception telescope.

This study is funded by the DGAC

References

Atmosphere, U. S.: US standard atmosphere, National Oceanic and Atmospheric Administration, 1976.

Augere, B., Besson, B., Fleury, D., Goular, D., Planchat, C., and Valla, M.: 1.5 µm lidar anemometer for true air speed, angle of sideslip, and angle of attack measurements on-board Piaggio P180 aircraft, Measurement Science and Technology, 27, 054 002, https://doi.org/10.1088/0957-0233/27/5/054002, 2016.

Baker, W. E., Emmitt, G. D., Robertson, F., Atlas, R. M., Molinari, J. E., Bowdle, D. A., Paegle, J., Hardesty, R. M., Menzies, R. T., Krishnamurti, T. N., Brown, R. A., Post, M. J., Anderson, J. R., Lorenc, A. C., and McElroy, J.: Lidar-Measured Winds from Space: A Key Component for Weather and Climate Prediction, Bulletin of the American Meteorological Society, 76, 869 – 888, https://doi.org/10.1175/1520-0477(1995)076<0869:LMWFSA>2.0.CO;2, 1995.

Baker, W. E., Atlas, R., Cardinali, C., Clement, A., Emmitt, G. D., Gentry, B. M., Hardesty, R. M., Källén, E., Kavaya, M. J., Langland, R., Ma, Z., Masutani, M., McCarty, W., Pierce, R. B., Pu, Z., Riishojgaard, L. P., Ryan, J., Tucker, S., Weissmann, M., and Yoe, J. G.: Lidar-Measured Wind Profiles: The Missing Link in the Global Observing System:, Bulletin of the American Meteorological Society, 95, 543 – 564, https://doi.org/10.1175/BAMS-D-12-00164.1, 2014.

Boulant, T. et al.: In process.

Bruneau, D.: Mach–Zehnder interferometer as a spectral analyzer for molecular Doppler wind lidar, Appl. Opt., 40, 391–399, https://doi.org/10.1364/AO.40.000391, 2001.

Bruneau, D.: Fringe-imaging Mach-Zehnder interferometer as a spectral analyzer for molecular Doppler wind lidar, Appl. Opt., 41, 503–510, https://doi.org/10.1364/AO.41.000503, 2002.

Bruneau, D. and Pelon, J.: Simultaneous measurements of particle backscattering and extinction coefficients and wind velocity by lidar with a Mach–Zehnder interferometer: principle of operation and performance assessment, Applied Optics, 42, 1101–1114, 2003.

Bruneau, D. and Pelon, J.: A new lidar design for operational atmospheric wind and cloud/aerosol survey from space, Atmospheric Measurement Techniques, 14, 4375–4402, https://doi.org/10.5194/amt-14-4375-2021, 2021.

Cezard, N.: Etude de faisabilité d'un lidar Rayleigh-Mie pour la mesure à courte distance de la vitesse de l'air de sa température et de sa densité., Theses, Ecole Polytechnique X, https://pastel.archives-ouvertes.fr/pastel-00004485, 2008.

Cézard, N., Dolfi-Bouteyre, A., Huignard, J.-P., and Flamant, P. H.: Performance evaluation of a dual fringe-imaging Michelson interferometer for air parameter measurements with a 355 nm Rayleigh-Mie lidar, Applied optics, 48, 2321–2332, 2009.

Fournier, H., Massioni, P, Tu Pham, M., Bako, L., Vernay, R., and Colombo, M.: Robust Gust Load Alleviation of Flexible Aircraft Equipped with Lidar, Journal of Guidance, Control, and Dynamics, 45, 58–72, https://doi.org/10.2514/1.G006084, 2022.

Fujii, T. and Fukuchi, T.: Laser Remote Sensing, CRC Press, 2005.

Garnier, A. and Chanin, M. L.: Description of a Doppler rayleigh LIDAR for measuring winds in the middle atmosphere, Applied Physics B, 55, 35–40, https://doi.org/10.1007/BF00348610, 1992.

Giez, A., Mallaun, C., Nenakhov, V., and Zöger, M.: Calibration of a nose boom mounted airflow sensor on an atmospheric research aircraft by inflight Maneuvers, 2021.

Hamamatsu R10721-210: https://www.hamamatsu.com/content/dam/hamamatsu-photonics/sites/documents/99_SALES_LIBRARY/etd/H10720_H10721_TPMO1062E.pdf.

Hamamatsu S5971: https://www.hamamatsu.com/content/dam/hamamatsu-photonics/sites/documents/99_SALES_LIBRARY/ssd/s5971_etc_kpin1025e.pdf.

Hamamatsu S9075: https://www.hamamatsu.com/content/dam/hamamatsu-photonics/sites/documents/99_SALES_LIBRARY/ssd/
470   s12053-02_etc_kapd1001e.pdf.

Herbst, J. and Vrancken, P.: Design of a monolithic Michelson interferometer for fringe imaging in a near-field, UV, direct-detection Doppler wind lidar, Applied Optics, 55, 6910–6929, 2016.

Karabulut Kurt, G., Khoshkholgh, M. G., Alfattani, S., Ibrahim, A., Darwish, T. S. J., Alam, M. S., Yanikomeroglu, H., and Yongacoglu, A.: A Vision and Framework for the High Altitude Platform Station (HAPS) Networks of the Future, IEEE Communications Surveys &
475   Tutorials, 23, 729–779, https://doi.org/10.1109/COMST.2021.3066905, 2021.

Kikuchi, R., Misaka, T., Obayashi, S., and Inokuchi, H.: Real-time estimation of airflow vector based on lidar observations for preview control, Atmospheric Measurement Techniques, 13, 6543–6558, 2020.

Liméry, A.: Étude et réalisation d'un lidar Raman pour la détection d'hydrogène et de vapeur d'eau dans une alvéole de stockage de colis radioactifs, Theses, Université Paris Saclay (COmUE), https://tel.archives-ouvertes.fr/tel-01838254, 2018.

480 Lux, O., Wernham, D., Bravetti, P., McGoldrick, P., Lecrenier, O., Riede, W., D'Ottavi, A., De Sanctis, V., Schillinger, M., Lochard, J., et al.: High-power and frequency-stable ultraviolet laser performance in space for the wind lidar on Aeolus, Optics letters, 45, 1443–1446, 2020.

Mondin, L., Wernham, D., Era, F., Kheyrandish, H., Bolkhovitinov, A., Mateo, A. B., Ciapponi, A., Heese, C., Ivanov, T., Hippler, M., et al.: Caveats and pitfalls of high energy UV laser operation on ground, in: International Conference on Space Optics—ICSO 2016, vol.
485   10562, pp. 524–532, SPIE, 2017.

Regan, C. D. and Jutte, C. V.: Survey of Applications of Active Control Technology for Gust Alleviation and New Challenges for Lighter-weight Aircraft, 2012.

Smith, J. A. and Chu, X.: Investigation of a field-widened Mach–Zehnder receiver to extend Fe Doppler lidar wind measurements from the thermosphere to the ground, Applied Optics, 55, 1366–1380, 2016.

490 Wilson, D. K.: Turbulence models and the synthesis of random fields for acoustic wave propagation calculations, Tech. rep., ARMY RE-SEARCH LAB ADELPHI MD, 1998.

Wirth, M., Fix, A., Mahnke, P., Schwarzer, H., Schrandt, F., and Ehret, G.: The airborne multi-wavelength water vapor differential absorption lidar WALES: system design and performance, Applied Physics B, 96, 201–213, 2009.

Witschas, B., Lemmerz, C., Lux, O., Marksteiner, U., Reitebuch, O., Weiler, F., Fabre, F., Dabas, A., Flament, T., Huber, D., and Vaughan, M.:
495   Spectral performance analysis of the Aeolus Fabry–Pérot and Fizeau interferometers during the first years of operation, Atmospheric Measurement Techniques, 15, 1465–1489, https://doi.org/10.5194/amt-15-1465-2022, 2022.